ARTICLE   OPEN

Check for updates

Intertwined electronic and magnetic structure of the van-der-Waals antiferromagnet $Fe_2P_2S_6$

A. Koitzsch [1 ✉], T. Klaproth[1], S. Selter[1], Y. Shemerliuk [1], S. Aswartham [1], O. Janson[1], B. Büchner[1,2] and M. Knupfer[1]

Many unusual and promising properties have been reported recently for the transition metal trichalcogenides of the type MPS_3 (M = V, Mn, Fe, Ni …), such as maintaining magnetic order to the atomically thin limit, ultra-sharp many-body excitons, metal-insulator transitions and, especially for $Fe_2P_2S_6$, giant linear dichroism among others. Here we conduct a detailed investigation of the electronic structure of $Fe_2P_2S_6$ using angle-resolved photoemission spectroscopy, **q**-dependent electron energy loss spectroscopy, optical spectroscopies and density functional theory. $Fe_2P_2S_6$ is a Mott insulator with a gap of $E_{gap} \approx 1.4$ eV and zigzag antiferromagnetism below $T_N = 119$ K. The low energy excitations are dominated by Fe 3d states. Large and sign-changing linear dichroism is observed. We provide a microscopic mechanism explaining key properties of the linear dichroism based on the correlated character of the electronic structure, thereby elucidating the nature of the spin-charge coupling in $Fe_2P_2S_6$ and related materials.

npj Quantum Materials (2023)8:27 ; https://doi.org/10.1038/s41535-023-00560-z

INTRODUCTION

Transition metal thiophosphates of the form MPS_3 (M = Mn, Fe, Ni, Zn …) have attracted ample scientific attention recently, after magnetic 2D materials have been established as its own flourishing subtopic within 2D research[1,2] and after it was recognized that the thiophosphates exhibit a layered crystal structure that can be mechanically exfoliated while maintaining magnetic order down to atomically thin layers[3–7]. Subsequently, a number of surprising phenomena have been found that reflect their rich physics not necessarily restricted to the atomic 2D limit[8]. In particular, an unusual ultra sharp exciton was discovered in $Ni_2P_2S_6$, probably related to the underlying correlated electronic structure[9]. $Fe_2P_2S_6$, on the other hand, shares with $Ni_2P_2S_6$ the zigzag magnetic order below $T_N = 119$ K (158 K for $Ni_2P_2S_6$)[10] but became especially relevant for the observation of giant optical linear dichroism. The dichroism is linked to the spin structure since it vanishes above T_N. But how exactly, i.e., on a microscopic level, the zigzag pattern is related to the optical properties remains elusive.

In this work we elucidate the electronic structure of $Fe_2P_2S_6$, in particular the origin of the optical anisotropy and its connection with the magnetic order. To this end we combine photoemission spectroscopy with electron energy loss spectroscopy (EELS) and optical spectroscopy as well as density functional theory (DFT) calculations. We observe the presence of large linear dichroism also for optical transmission measurements. Based on thorough understanding of the band structure and the dielectric function we develop a microscopic model of the underlying electronic processes and how they are connected to the magnetic order.

The electronic structure of $Fe_2P_2S_6$ and other thiophosphates has been studied before. Initially, $Fe_2P_2S_6$ had been characterized as a magnetic semiconductor with a gap of about 1.5 eV[11]. First photoemission experiments on $Fe_2P_2S_6$ date back to 1982[12]. In this time, the research on layered thiophosphates was motivated by possible applications as cathode materials for batteries based on Li intercalation. The electronic structure has been described based on an ionic picture: there are covalently bonded $(P_2S_6)^{4-}$

units and M^{2+} ions with localized 3d levels substantially influenced by correlation effects. These localized states of the unfilled M 3d orbitals may appear inside the gap or at the top of the valence band[13,14]. However, to consider Fe 3d electrons as a separate manifold in the purely ionic picture is too simplistic a view as has been shown by subsequent resonant and angle-resolved photo-emission[15]. Resonant photoemission was also useful to establish the Mott character of the gap of $Fe_2P_2S_6$ contrary to the charge transfer character of $Ni_2P_2S_6$[16–18]. Interestingly, the Mott gap collapses upon the application of high pressure[19], and the spin state of Fe^{2+} possibly changes[20,21].

Yet, the main source of growing interest in $Fe_2P_2S_6$ are the remarkable optical properties of this material. The large and tunable linear dichroism[22,23], giant surface second harmonic generation[24] and air stable ultra-broad spectral photo-response[25] may hold prospects for device implementation of various kinds, which calls for detailed analysis of the underlying electronic processes.

Here we provide this insight: being a Mott insulator the low energy electronic structure is found to be dominated by Fe 3d states. The combination of local spin arrangement and zigzag antiferromagnetic order induces a direction dependence of possible electronic transitions that gives rise to a strongly anisotropic dielectric function.

RESULTS

Photoemission spectroscopy

Figure 1a presents angle integrated UPS measurements of the valence band using He I ($h\nu = 21.2$ eV) and He II ($h\nu = 40.8$ eV) photons. In addition to the experimental data we plot partial density of states of S 3p and Fe 3d obtained by DFT + U.

The main features of the spectrum are consistent with earlier reports[13,15]. The valence band shows a partition into three regions labeled A, B and C, which all have their own fine structure. Region A is lowest in energy and as such most important for the optical and electronic properties of the material. It consists mainly of Fe
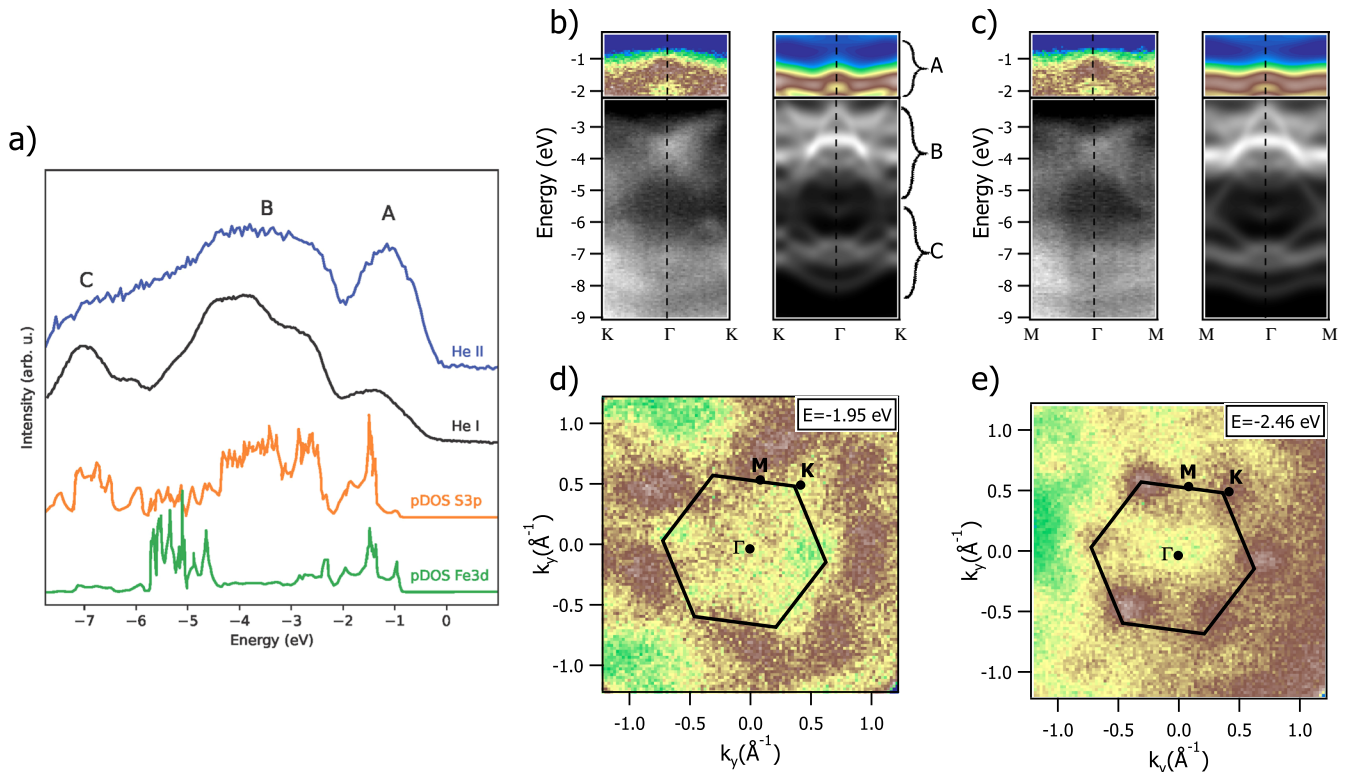
Fig. 1 Photoemission spectroscopy results and DFT. a Background corrected valence band photoemission spectra of $Fe_2P_2S_6$ obtained using He I ($hv = 21.2$ eV) and He II ($hv = 40.8$ eV) radiation in comparison to calculated partial density of states (PDOS). The energy zero has been set to the valence band maxima for the experimental data. The energy axis of the PDOS has been adjusted for best comparison to experiment. **b, c** Energy distribution maps along ΓK and ΓM in comparison to DFT results. The low energy part is presented at its own color scale to enhance weak features. **d, e** Constant energy maps at $E = -1.95$ eV and $E = -2.46$ eV. Black hexagon: surface Brillouin zone constructed using experimental structural data.

$3d$ states, which follows from its photon energy dependence: it is enhanced for He II excitation as compared to He I. He II excitation strongly favors Fe $3d$ emission according to cross section tables, whereas He I is dominated by S $3p$ weight[26]. The latter is well reproduced by the S $3p$ PDOS. The comparison of the He II spectrum to the Fe $3d$ PDOS on the other hand reveals some discrepancies, in particular a relative upshift of the Fe $3d$ states. However, the Fe $3d$ character of the valence band states closest to E_F is borne out by the DFT + U calculations. The dominating Fe $3d$ character of feature A is consistent with previous multiplet calculations[15]. Within cubic symmetry it corresponds to the $^6A_{1g}$ groundstate of the d^5 configuration that remains after one d electron is photoemitted from the high spin $t_{2g}^4 e_g^2$ configuration of the initial d^6 state. Also resonant photoemission found that the low energy region is dominated by Fe $3d^5$ final state (rather than by Fe $3d^6$L where L stands for a ligand hole) classifying $Fe_2P_2S_6$ as a Mott insulator with $\Delta_{pd} > U$[16,18]. Reported values for U derived from previous DFT + U or multiplet calculations are in the range $U = 2.2$–3.0 eV[18,25,27].

Region B is more of mixed S $3p$/Fe $3d$ character and, in a local description, contains most of the excited d^5 multiplet terms. Region C comprises of significantly less Fe $3d$ character, which is seen both in the He II spectrum and in the Fe $3d$ PDOS.

Now we consider angle resolved photoemission results. Figure 1b, c presents energy distribution maps (EDM) along the ΓK and ΓM direction measured by He I excitation together with DFT results. Again the three main components of the valence band, A, B and C, are easily distinguished throughout the Brillouin zone and do not mix much.

Regions B and C exhibit dispersing features, indicating delocalization of the electronic states. The comparison to DFT

results based on the S $3p$ weighted band structure is satisfactory. Region A displays less dispersion than region B and C but still the dispersion is clearly visible indicating some nonlocal character. The band appears to be shifted up with respect to DFT but some correspondence of the spectral shape is present. According to the full band structure the valence band maximum (VBM) is situated at Γ, which is also consistent with the photoemission results.

Figure 1d, e shows constant energy intensity maps at two selected energies. $Fe_2P_2S_6$ crystallizes in the monoclinic C 2/m space group. But the individual layers have hexagonal symmetry and form a honeycomb lattice. The latter is clearly observed in the distribution of photoemission intensity. Figure 1d contains the surface Brillouin zone obtained from structural data in ref. [27]. Agreement is found with the distribution of photoemission intensity. The energy difference of the two constant energy maps is about 0.5 eV but they look very different, indicating again substantial in-plane dispersion.

Electron energy loss spectroscopy

Now we shift our attention from the one particle spectral function to the two-particle response obtained by EELS. EELS measures the loss function defined as $L = \text{Im}[-1/\epsilon]$, where ϵ is the complex dielectric function. Low energy EEL spectra often resemble optical responses like optical conductivity or absorption measurements. Our EELS measurements are done in transmission and, therefore, bulk sensitive. Figure 2a presents EELS data over a wide energy range. The most prominent feature is a peak at $E = 20.1$ eV, which belongs to the volume plasmon. Earlier surface sensitive studies based on EELS in reflection found this peak at $E = 21.0$–21.2 eV[28,29]. A recent TEM-EELS study of $MnPS_3$ obtained $E \approx 19$ eV[30]. The energy of the bulk plasmon in Fig. 2a is
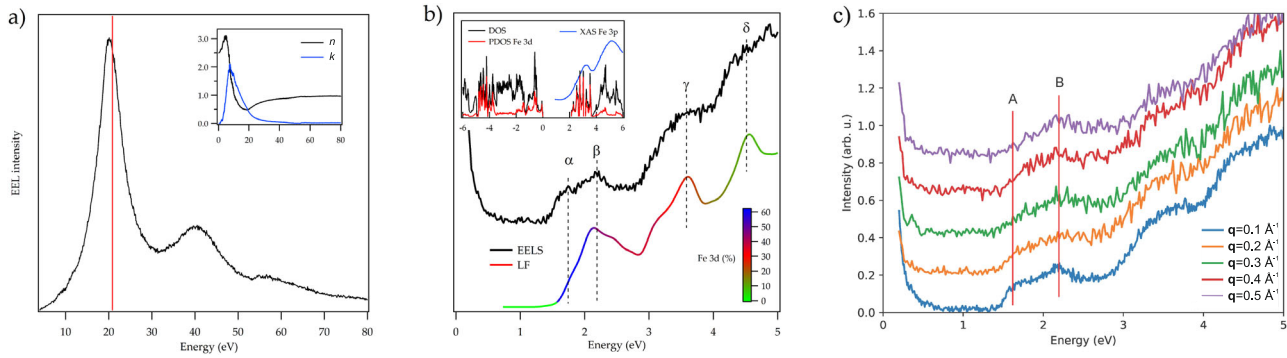
Fig. 2 Electron energy loss spectroscopy results. a EEL intensity over a wide energy range. The peak at $E \approx 20$ eV belongs to the bulk plasmon, with higher orders around 40 and 60 eV. The red vertical line marks the location of the plasma energy in the free electron limit (see text). Inset: Optical constants obtained by a Kramers-Kronig-analysis (see text for details). **b** Low energy EELS intensity in the optical limit ($\mathbf{q} = 0.1$ Å^{-1}) vs. loss function obtained by DFT. Theory curve has been shifted horizontally for better comparison with experiment. Color scale corresponds to the degree of Fe 3d character. Inset: Density of states (DOS) together with x-ray absorption data at the Fe 3p edge from ref. [15]. **c** $\mathbf{q}$-dependent EELS data.

reasonably close to the free electron plasma energy given by $\omega_p^2 = Ne^2/(\epsilon_0 m_e)$, where N is the density of outer-shell valence electrons, m_e is the electron mass, and ϵ_0 is the permittivity of free space. At higher energy the second and third order of the volume plasmon are present. In addition, a weak feature at $E \approx 55$ eV can be assigned to the Fe 3p edge.

We have conducted a Kramers-Kronig analysis (KKA) and obtained the complex refractive index (inset). The low energy refractive index has been normalized to ≈ 2.5, a value reported previously[31]. Such an analysis is not without approximations, e.g., concerning the treatment of multielectron scattering. The results for the low energy extinction coefficient compare well to earlier studies[25].

Figure 2b presents a measurement of the EEL spectrum at low energy at $T = 20$ K. At the very lowest energy contributions from the elastically scattered intensity is seen. A sharp intensity onset is found at $E \approx 1.5$ eV, which has been associated with the principal bandgap. A Tauc plot analysis yields $E_{gap} = 1.38$ eV in agreement with literature data[11,25,27,29] (see Supplementary Note 3 for details).

Above the bandgap several sharp features are discernible labeled α, β, γ, δ in Fig. 2b. They compare well to the loss function calculated from the DFT band structure (see Supplementary Note 6 for details). In order to get deeper understanding on the origin of these features we consider again the density of states (upper inset). The unoccupied DOS shows agreement with x-ray absorption measurements at the Fe 3p edge. At top of the valence band and the bottom of the conduction band the total DOS is dominated by Fe 3d states as it is expected for a Mott insulator. This implies that the lowest interband transitions are of intersite $d^6 d^6 \rightarrow d^5 d^7$ type. Hence, electronic transitions across the gap mainly involve iron. This can be directly monitored by considering the joint density of states (JDOS). The JDOS is proportional to ϵ_2. By comparing the JDOS obtained from the total DOS and obtained from the Fe 3d PDOS alone, we derive the Fe 3d, or Mott character, of the loss function shown as color scale in Fig. 2b (see the Supplementary Note 1 for details). The iron character is most pronounced directly above the gap onset, especially for peak α and, already to a lesser degree, for peak β. For higher energy it monotonously decreases. This is consistent with a calculation of the Fe 3d part of the loss function based on a Wannier projection scheme (see Supplementary Note 6 for details). The increasing intensity toward higher energy in the experimental data and theory reflects the large S 3p PDOS associated with charge transfer transitions and the rising flank of the massive bulk plasmon.

We have also studied the $\mathbf{q}$-dependence of the EELS response shown in Fig. 2c. Note that non-vertical transitions are not directly accessible by standard optical experiments. The lowest energy

feature α disperses to higher energies with increasing $\mathbf{q}$ and looses spectral weight. This indicates the presence of a direct gap. The dispersion of feature α is in the order of a couple of 100 meV matching approximately the degree of dispersion seen by ARPES for the lowest energy valence band. This and the flat, dispersion-less character of β confirm the purported Fe 3d character of the low energy region.

Optical spectroscopy

We resume studying the dielectric properties of Fe$_2$P$_2$S$_6$ by optical spectroscopy, in particular the linear dichroism. Figure 3a presents polarization and temperature dependent transmission measurements of an exfoliated Fe$_2$P$_2$S$_6$ flake (see Supplementary Note 4 for an optical image of the flake). The transmission exhibits a maximum at $E \approx 1.3$ eV. The overall shape of the transmission spectra can be understood by comparison to the EEL spectrum (Fig. 3c). We consider $1 - $ Transmission, which corresponds to the absorption under the approximation that the reflection can be neglected. The absorption is proportional to ϵ_2, which also dominates the EELS response. The lineshapes resemble each other in Fig. 3c. It becomes clear that the energy region of the transmission spectra between $E = 1.3–2.5$ eV belongs to optical excitations across the Mott gap. The transmission is low in this energy region because transitions across the bandgap are possible. The small upturn at lowest energy $E \approx 1$ eV is due to onsite dd excitations[12,32] and thin film interference effects. The spectral shape is consistent with earlier optical measurements[13,25,27,32]. In order to estimate the thickness of the flake we have fitted the transmission spectrum to a thin film interference model using the optical constants from Fig. 2a as input parameters. We obtain a thickness of about 390 nm (see Supplementary Note 2 for details).

Now we consider the linear dichroism, i.e., the dependence of the transmission on polarization direction. Very large linear dichroism has been reported in reflection recently for Fe$_2$P$_2$S$_6$ below T_N[22,23]. The temperatures in Fig. 3a ($T = 79$ K and $T = 173$ K) are well below and well above the bulk Neel temperature ($T_N = 117$ K). "0"" refers to the situation where the polarization is parallel to the direction of the spin chains (parallel to a in Fig. 3a (inset)). We have assigned the crystal orientation by comparison of the experimental transmission to our optical simulations using the polarization dependent dielectric function obtained by DFT and by comparison to literature[22] (see Fig. 4e and Supplementary Note 7 for details). We observe that the transmission is almost independent of the polarization direction above T_N. Below T_N clear differences develop, most pronounced in the energy range $E = 1.5–2.0$ eV, that means a linear dichroism is present (Fig. 3a) and its maximum coincides with feature α (Fig. 2b).
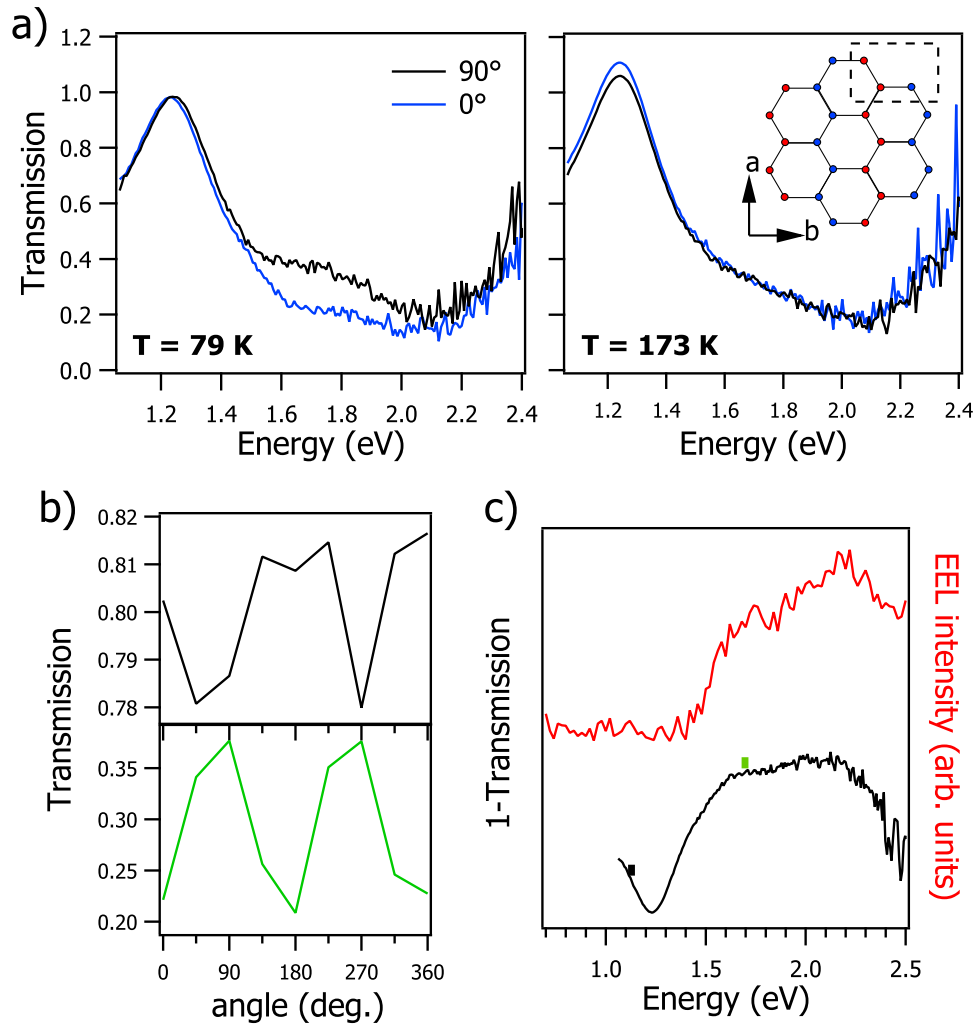
Fig. 3 **Polarization dependent optical spectroscopy. a** Polarization and temperature dependent optical transmission measurements. Inset: Sketch of the in plane crystal structure. Blue and red color corresponds to opposite spin orientation indicating the zigzag-AFM order. The dashed rectangle is shown again in Fig. 4 in an expanded version. **b** Polarization angle dependence of the transmission at $E = 1.1$ eV (upper panel) and 1.7 eV (lower panel). **c** Comparison of EELS data and 1-Transmission. Colored bars correspond to the angle scans in (**b**).

Closer inspection of Fig. 3a ($T = 79$ K) reveals that the transmission maxima at $E \approx 1.2$ eV are slightly shifted against each other depending on the polarization, i.e., the dichroism changes sign at low energy.

In Fig. 3b we show the transmission as a function of polarization angle at two different energies highlighted by colored bars in Fig. 3c corresponding to $E = 1.7$ eV where the linear dichroism appears to be maximal and at $E = 1.1$ eV (see Supplementary Note 5 for an extended dataset). At $E = 1.7$ eV large oscillations appear below T_N and follow a periodicity of 180°, consistent with the zigzag magnetic order. Interestingly, a small effect is also seen at low energy ($E = 1.1$ eV). The linear dichroism keeps its 180° periodicity for $E = 1.1$ eV but reverses sign. The origin of this peculiar sign change behavior is again thin film interference[23]. The position of the maxima/minima of the reflection or absorption of a flake of a given thickness depend on the refractive index which depends on the direction.

DISCUSSION
In the following we discuss the physical origin of the observed large optical anisotropy which is linked to the magnetic anisotropy. Optical linear dichroism is not a rare phenomenon but the magnitude and character of the effect observed for

Fe$_2$P$_2$S$_6$ are exceptional. Related van-der-Waals materials black phosphorus and ReS$_2$ show large in-plane linear dichroism but there the linear dichroism originates in the anisotropy of the crystal lattice[33,34]. A structural phase transition has been reported for Fe$_2$P$_2$S$_6$ accompanying the magnetic order with a distortion of the honeycomb lattice by 0.2%[35]. However, no such effect is known for the related compound Ni$_2$P$_2$S$_6$ suggesting that the magnetic order is directly responsible for the linear dichroism and not indirectly via magneto-crystalline coupling.

The energy range where the linear dichroism is large coincides with the excitations across the bandgap of Fe $3d$ character, which root in electronic intersite transitions of the type $d^6 d^6 \rightarrow d^5 d^7$. Figure 4a shows the spin states including the crystal field levels at various lattice points below T_N. There are two types of nearest-neighbor intersite transitions: parallel to the spin chain and perpendicular to it and they are qualitatively different. In addition, next-nearest neighbor and cross-hexagon hoppings parallel and perpendicular to the spin chain could be of relevant magnitude but are neglected in Fig. 4a for clarity.

Figure 4b shows a schematic density of state representation of the situation in (a). The low energy electronic structure consists of a filled lower Hubbard band and an empty upper Hubbard band separated by U, both mainly of Fe $3d$ character. Spin conserving interband transitions are possible for the majority spin in x-
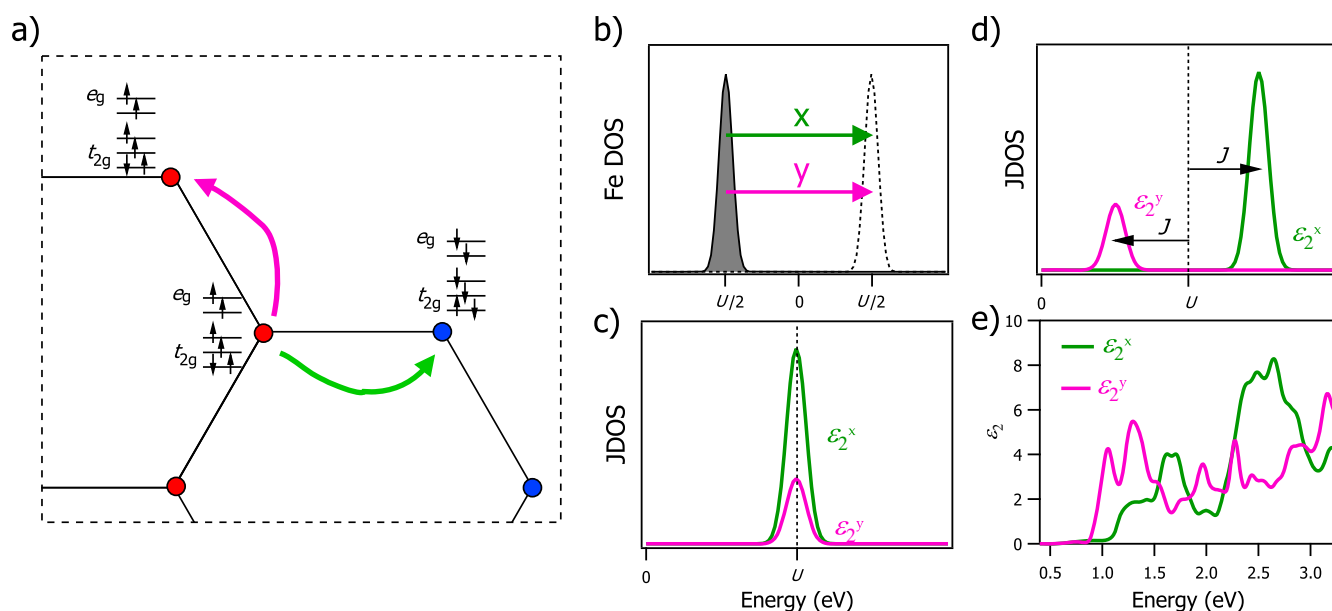
Fig. 4 Electronic structure and dielectric function. a Sketch of the local spin arrangement and possible intersite transitions parallel or perpendicular to the spin chain. Spin up and down is highlighted by red and blue. **b** Schematical Fe $3d$ DOS. **c** Joint density of states following from (**b**) respecting available phase space. **d** Same as (**c**) under consideration of exchange energy. **e** ϵ_2 calculated by DFT $+ U$.

direction only, because the y-direction is Pauli-blocked. For the minority spin the situation is reversed: it is possible along y and blocked along x. However, the available phase space for majority spin transitions is much larger than for minority spins. The JDOS that follow from (b) is shown in (c). Assuming JDOS $\propto \epsilon_2$ this translates into an anisotropic dielectric function. Besides the different phase space also the energy of the final states differs for majority vs. minority hopping channel. In particular, minority hopping leaves a high spin d^5 state behind ($\uparrow\uparrow\uparrow\uparrow\uparrow$), whereas the majority hopping leads to intermediate spin ($\uparrow\uparrow\uparrow\uparrow\downarrow$), resulting in an energy difference of $\sim 2J$ (see Supplementary Note 8 for a more precise treatment). The dielectric function that follows resembles the DFT result shown in (e) plus some background contribution from non Fe $3d$ bands, giving confidence to the underlying physical assumptions, in particular, the way the magnetic order dictates optical transitions. Note, that this simple model neglects nonlocal effects and multiplet splitting, which may influence the precise location of the final states.

In conclusion we have thoroughly studied the electronic and optical properties of $Fe_2P_2S_6$. It becomes clear that linear dichroism is intimately related to the correlated electronic structure of $Fe_2P_2S_6$ and to the zigzag arrangement of local moments below T_N. $Fe_2P_2S_6$ is a Mott insulator with a certain degree of delocalization of the $3d$ levels. The low energy interband transitions are of intersite dd character. The presence of large optical linear dichroism is confirmed, which changes sign depending on energy. A microscopic mechanism is provided explaining key properties of the linear dichroism based on the correlated character of the electronic structure of $Fe_2P_2S_6$. The key ingredients are that the nearest-neighbor hopping is dominated by t_{2g} orbitals, the Hund's rule favors hopping of minority electrons, and the Pauli principle forbids the inter-chain hopping.

METHODS

Crystal growth and sample preparation

$Fe_2P_2S_6$ crystals have been grown in a two step process: first, polycrystalline powder was obtained by solid state synthesis from the elements, then single crystal were grown from these polycrystalline precursors by chemical vapor transport. Details can be found in ref. [10].

For subsequent photoemission and optical measurements $Fe_2P_2S_6$ bulk crystals have been exfoliated using either scotch tape or poly-dimethylsiloxane (PDMS) sheets. In case of photoemission, scotch tape with a thin $Fe_2P_2S_6$ crystal was sticked to a piece of gold coated Si-wafer, removed under UHV conditions (5×10^{-10} mbar) and crystal flakes stuck to the wafer were measured. Optical experiments were performed on crystal flakes directly on top of the PDMS sheets.

Spectroscopic measurements

The photoemission data was measured using a NanoESCA system (Scienta Omicron) equipped with a HIS 13 helium lamp with an energy of 21.21 eV (He I) and 40.8 eV (He II) and an energy resolution ≤0.2 eV.

$Fe_2P_2S_6$ is an insulator and susceptible to charging effects under photoemission. While we have not observed detrimental effects concerning the spectral shape, moderate binding energy shifts are present. Hence, we refer the energy axis to the top of the valence band instead of the Fermi energy.

The EELS measurements were carried out using a purpose built transmission electron energy-loss spectrometer with a primary electron energy of 172 keV and energy and momentum resolutions of $\Delta E = 85$ meV and $\Delta q = 0.035$ Å^{-1}, respectively, at $T = 20$ K[36,37]. The films ($d \approx 100$ nm) were exfoliated by scotch tape. Subsequently, the films were mounted onto standard electron microscopy grids and transferred into the EELS spectrometer.

Optical transmission spectra were measured at temperatures down to 79 K using a Bruker VERTEX 80 V spectrometer with the Hyperion 2000 microscope extension with ×15 Schwarzschild objectives in normal transmission configuration and suitable polarization filters from Quantum Design. A tungsten-halogen lamp was employed as excitation source together with a Si-diode based detector. Cryogenic temperatures were reached by a N_2 flow cryostat (Linkam Scientific, FTIR 600).

DFT calculations

Density functional theory band-structure calculations were done using the full-potential local-orbital code FPLO[38] version 21. We used the experimental structure from ref. [39] as the structural input (see Supplementary Table 1). The primitive unit cell comprises only one Wyckoff position of Fe and thus can not account for an antiferromagnetic state. To construct a cell compatible with the experimentally observed[40] $\mathbf{q} = \left(0, \frac{1}{2}, \frac{1}{2}\right)$ magnetic structure, we doubled the primitive cell along the c-axis and subsequently symmetrized it. For the exchange and correlation potential, we use the generalized gradient approximation (GGA)[41] supplemented by the Hubbard-like local interaction term (DFT + U). All results presented in the manuscript were obtained using the Coulomb repulsion $U = 2.5$ eV, the Hund exchange $J_d = 1$ eV, and the fully localized limit as the double-counting correction. The dielectric function ε and loss function L were calculated using the built-in optics module of FPLO. All self-consistent calculations were performed on a k-mesh of $10 \times 10 \times 20$ points (557 points in the irreducible wedge).

DATA AVAILABILITY

The data that support the findings of this study are available from the corresponding author upon reasonable request.

REFERENCES

1. Huang, B. et al. Layer-dependent ferromagnetism in a van der Waals crystal down to the monolayer limit. *Nature* **546**, 270–273 (2017).
2. Gong, C. et al. Discovery of intrinsic ferromagnetism in two-dimensional van der Waals crystals. *Nature* **546**, 265–269 (2017).
3. Lee, J.-U. et al. Ising-type magnetic ordering in atomically thin FePS$_3$. *Nano Lett.* **16**, 7433–7438 (2016).
4. Kuo, C.-T. et al. Exfoliation and Raman spectroscopic fingerprint of few-layer NiPS$_3$ Van der Waals crystals. *Sci. Rep.* **6**, 20904 (2016).
5. Du, K.-z. et al. Weak Van der Waals stacking, wide-range band gap, and Raman study on ultrathin layers of metal phosphorus trichalcogenides. *ACS Nano* **10**, 1738–1743 (2016).
6. Chittari, B. L. et al. Electronic and magnetic properties of single-layer MPX_3 metal phosphorous trichalcogenides. *Phys. Rev. B* **94**, 184428 (2016).
7. Kim, K. et al. Suppression of magnetic ordering in XXZ-type antiferromagnetic monolayer NiPS$_3$. *Nat. Commun.* **10**, 345 (2019).
8. Shentcis, M. et al. Tunable free-electron x-ray radiation from van der waals materials. *Nat. Photon.* **14**, 686–692 (2020).
9. Kang, S. et al. Coherent many-body exciton in van der Waals antiferromagnet NiPS$_3$. *Nature* **583**, 785–789 (2020).
10. Selter, S. et al. Crystal growth and anisotropic magnetic properties of quasi-two-dimensional $(Fe_{1-x}Ni_x)_2P_2S_6$. *Phys. Rev. Mater.* **5**, 073401 (2021).
11. Brec, R., Schleich, D. M., Ouvrard, G., Louisy, A. & Rouxel, J. Physical properties of lithium intercalation compounds of the layered transition-metal chalcogenophosphites. *Inorg. Chem.* **18**, 1814–1818 (1979).
12. Piacentini, M., Khumalo, F., Leveque, G., Olson, C. & Lynch, D. X-ray photoemission and optical spectra of NiPS$_3$, FePS$_3$ and ZnPS$_3$. *Chem. Phys.* **72**, 61–71 (1982).
13. Piacentini, M. et al. Study of the valence bands of FePS$_3$ and NiPS$_3$ by resonant-photoemission spectroscopy. *Il Nuovo Cimento D* **4**, 444–452 (1984).
14. Ohno, Y. & Hirama, K. S K and P K absorption spectra and electronic structures of layered thiophosphates MPS$_3$. *J. Solid State Chem.* **63**, 258–266 (1986).
15. Choi, W.-K., Kneedler, E. & Kevan, S. D. Delocalization of the Fe 3d levels in the quasi-two-dimensional correlated insulator FePS$_3$. *Phys. Rev. B* **50**, 15276–15286 (1994).
16. Kamata, A. et al. Resonant 2 p–3 d photoemission measurement of MPS$_3$ (M=Mn, Fe, Ni). *J. Phys. Soc. Jpn.* **66**, 401–407 (1997).
17. Yan, M. et al. Correlations in the electronic structure of van der Waals NiPS$_3$ crystals: an X-ray absorption and resonant photoelectron spectroscopy study. *J. Phys. Chem. Lett.* **12**, 2400–2405 (2021).
18. Jin, Y., Yan, M., Kremer, T., Voloshina, E. & Dedkov, Y. Mott-Hubbard insulating state for the layered van der Waals FePX$_3$ (X: S, Se) as revealed by NEXAFS and resonant photoelectron spectroscopy. *Sci. Rep.* **12**, 735 (2022).
19. Haines, C. R. S. et al. Pressure-induced electronic and structural phase evolution in the van der Waals compound FePS$_3$. *Phys. Rev. Lett.* **121**, 266801 (2018).
20. Wang, F. et al. New frontiers on van der Waals layered metal phosphorous trichalcogenides. *Adv. Funct. Mat.* **28**, 1802151 (2018).
21. Coak, M. J. et al. Emergent magnetic phases in pressure-tuned van-der-Waals antiferromagnet FePS$_3$. *Phys. Rev. X* **11**, 011024 (2021).
22. Zhang, Q. et al. Observation of giant optical linear dichroism in a zigzag antiferromagnet Fe$_2$P$_2$S$_6$. *Nano Lett.* **21**, 6938–6945 (2021).
23. Zhang, H. et al. Cavity-enhanced linear dichroism in a van-der-Waals antiferromagnet. *Nat. Photon.* **16**, 311–317 (2022).
24. Ni, Z., Huang, N., Haglund, A. V., Mandrus, D. G. & Wu, L. Observation of giant surface second-harmonic generation coupled to nematic orders in the van der Waals antiferromagnet FePS$_3$. *Nano Lett.* **22**, 3283–3288 (2022).
25. Ramos, M. et al. Ultra-broad spectral photo-response in FePS$_3$ air-stable devices. *npj 2D Mater. Appl.* **5**, 19 (2021).
26. Yeh, J. & Lindau, I. Atomic subshell photoionization cross sections and asymmetry parameters: 1≤ z ≤ 103. *At. Data Nucl. Data Tables* **32**, 1–155 (1985).
27. Budniak, A. K. et al. Spectroscopy and structural investigation of iron phosphorus trisulfide-FePS$_3$. *Adv. Opt. Mat.* **10**, 2102489 (2022).
28. Ohno, Y. Systematic EELS study of layered metal-phosphor-trisulfides MPS$_3$ (M = Mg, Mn, Fe, Ni, Zn, Cd). *Solid State Comm.* **67**, 1089–1092 (1988).
29. Abbati, I., Mariani, C., Chemelli, C. & Scagliotti, M. Vibrational and electronic properties of FePS$_3$ studied by HREELS and EELS. *Surf. Sci.* **281**, 127–132 (1993).
30. Kinyanjui, M. K., Koester, J., Boucher, F., Wildes, A. & Kaiser, U. Spectroscopic properties of a freestanding MnPS$_3$ single layer. *Phys. Rev. B* **98**, 035417 (2018).
31. Piacentini, M., Khumalo, F., Olson, C., Anderegg, J. & Lynch, D. Optical transitions, XPS, electronic states in NiPS$_3$. *Chem. Phys.* **65**, 289–304 (1982).
32. Joy, P. A. & Vasudevan, S. Optical-absorption spectra of the layered transition-metal thiophosphates MPS$_3$ (M=Mn, Fe, and Ni). *Phys. Rev. B* **46**, 5134–5141 (1992).
33. Mao, N. et al. Optical anisotropy of black phosphorus in the visible regime. *J. Am. Chem. Soc.* **138**, 300–305 (2016).
34. Wang, Y. Y. et al. In-plane optical anisotropy in ReS$_2$ flakes determined by angle-resolved polarized optical contrast spectroscopy. *Nanoscale* **11**, 20199–20205 (2019).
35. Jernberg, P., Bjarman, S. & Wäppling, R. FePS$_3$: a first-order phase transition in a "2D" Ising antiferromagnet. *J. Magn. Magn. Mater.* **46**, 178–190 (1984).
36. Fink, J. Recent developments in energy-loss spectroscopy. *Adv. Electron. Electron Phys.* **75**, 121–232 (1989).
37. Roth, F., König, A., Fink, J., Büchner, B. & Knupfer, M. Electron energy-loss spectroscopy: a versatile tool for the investigations of plasmonic excitations. *J. Electron. Spectrosc. Relat. Phenom.* **195**, 85–95 (2014).
38. Koepernik, K. & Eschrig, H. Full-potential nonorthogonal local-orbital minimum-basis band-structure scheme. *Phys. Rev. B* **59**, 1743–1757 (1999).
39. Brec, R., Ouvrard, G., Louisy, A. & Rouxel, J. Proprietes structurales de phases M^{II}PX$_3$ (X= S, Se). *Ann. Chim.* **5**, 499 (1980).
40. Lançon, D. et al. Magnetic structure and magnon dynamics of the quasi-two-dimensional antiferromagnet FePS$_3$. *Phys. Rev. B* **94**, 214407 (2016).
41. Perdew, J. P., Burke, K. & Ernzerhof, M. Generalized gradient approximation made simple. *Phys. Rev. Lett.* **77**, 3865–3868 (1996).

AUTHOR CONTRIBUTIONS

T.K. carried out the photoemission and EELS experiments. T.K. and A.K. performed the photoemission and EELS data analysis. A.K. carried out the optical experiments and analysis. DFT calculations have been provided by O.J. Samples have been grown and characterized by S.S., Y.S. and S.A. A.K. wrote the manuscript with input from all authors.

COMPETING INTERESTS

The authors declare no competing interests.

ADDITIONAL INFORMATION

Supplementary information The online version contains supplementary material available at https://doi.org/10.1038/s41535-023-00560-z.

Correspondence and requests for materials should be addressed to A. Koitzsch.

Reprints and permission information is available at http://www.nature.com/reprints

Publisher's note Springer Nature remains neutral with regard to jurisdictional claims in published maps and institutional affiliations.